PAPER • OPEN ACCESS

Raman study of layered breathing kagome lattice semiconductor Nb$_3$Cl$_8$

To cite this article: Dylan A Jeff *et al* 2023 *2D Mater.* **10** 045030

View the article online for updates and enhancements.

2D Materials

PAPER

Raman study of layered breathing kagome lattice semiconductor Nb$_3$Cl$_8$

Dylan A Jeff[1,2], Favian Gonzalez[1,2], Kamal Harrison[1,2], Yuzhou Zhao[3,4], Tharindu Fernando[4], Sabin Regmi[1], Zhaoyu Liu[4], Humberto R Gutierrez[5], Madhab Neupane[1], Jihui Yang[3], Jiun-Haw Chu[4], Xiaodong Xu[3,4], Ting Cao[3] and Saiful I Khondaker[1,2,*]

1 Department of Physics, University of Central Florida, Orlando, FL 32816, United States of America
2 NanoScience Technology Center, University of Central Florida, Orlando, FL 32826, United States of America
3 Department of Materials Science and Engineering, University of Washington, Seattle, WA 98195, United States of America
4 Department of Physics, University of Washington, Seattle, WA 98195, United States of America
5 Department of Physics, University of South Florida, Tampa, FL 33620, United States of America
* Author to whom any correspondence should be addressed.

E-mail: saiful@ucf.edu

Abstract

Niobium chloride (Nb$_3$Cl$_8$) is a layered two-dimensional semiconducting material with many exotic properties including a breathing kagome lattice, a topological flat band in its band structure, and a crystal structure that undergoes a structural and magnetic phase transition at temperatures below 90 K. Despite being a remarkable material with fascinating new physics, the understanding of its phonon properties is at its infancy. In this study, we investigate the phonon dynamics of Nb$_3$Cl$_8$ in bulk and few layer flakes using polarized Raman spectroscopy and density-functional theory (DFT) analysis to determine the material's vibrational modes, as well as their symmetrical representations and atomic displacements. We experimentally resolved 12 phonon modes, five of which are A_{1g} modes while the remaining seven are E_g modes, which is in strong agreement with our DFT calculation. Layer-dependent results suggest that the Raman peak positions are mostly insensitive to changes in layer thickness, while peak intensity and full width at half maximum are affected. Raman measurements as a function of excitation wavelength (473–785 nm) show a significant increase of the peak intensities when using a 473 nm excitation source, suggesting a near resonant condition. Temperature-dependent Raman experiments carried out above and below the transition temperature did not show any change in the symmetries of the phonon modes, suggesting that the structural phase transition is likely from the high temperature $P\bar{3}m1$ phase to the low-temperature $R\bar{3}m$ phase. Magneto-Raman measurements carried out at 140 and 2 K between -2 and 2 T show that the Raman modes are not magnetically coupled. Overall, our study presented here significantly advances the fundamental understanding of layered Nb$_3$Cl$_8$ material which can be further exploited for future applications.

1. Introduction

Nb$_3$Cl$_8$ is a member of the niobium halide (Nb$_3X_8$, $X =$ Cl, Br, I) family of layered two-dimensional (2D) materials that crystallize in a breathing kagome crystal lattice [1]. They are shown to be semiconducting through angle-resolved photoemission spectroscopy (ARPES) measurements on bulk [2, 3], and have

visible and infrared light absorbing capabilities. This family of materials recently garnered attention due to the effects that the breathing kagome lattice has on the material's band structure and magnetic orderings. Topological flat bands in the electronic band structures of Nb$_3$Cl$_8$ and Nb$_3$I$_8$ have been theoretically predicted and experimentally observed via ARPES [2, 3]. This exotic electronic band structure is linked to

the unique geometry of the kagome crystal lattice, which causes the localization of electrons within the hexagons formed by the corners of the niobium trimers. One of the effects that the kagome lattice in this system has on the magnetic orderings takes the form of magnetic frustration, where the material does not feature a single lowest energy state for the orientation of its spins [4–6]. At low temperatures, the crystal symmetry of Nb_3Cl_8 changes due to the unequal distribution of electrical charge between different layers of Nb trimers in the lattice. This results in a buckling of Cl layers and a rearrangement of the stacking order, which overcomes the magnetic frustration. As a result, Nb3Cl8 forms a nonmagnetic singlet ground state. This change in crystal symmetry is seen as the crystal changes from trigonal $P\bar{3}m1$ at high temperatures to a predominantly monoclinic $C2/m$ at low temperatures [4]. However, other studies suggested that the low-temperature phase is $R\bar{3}m$ symmetric instead [5, 7]. Additionally, Nb_3Cl_8 features favorable cleavage energies for the separation of layers from the bulk crystal, speaking to the feasibility of its exfoliation to thinner layers [8]. As a semiconductor with a moderate band gap of 1.12 eV, great light absorption, and increased conductivity in thin layers; Nb_3Cl_8 is a prime candidate for future electronic, optoelectronic, and spintronic device applications [2, 8]. Despite being an interesting material with many exotic electronic and magnetic properties, experimental investigations of the optical and vibrational properties of Nb_3Cl_8 such as the number of phonon modes, their symmetry assignments, atomic displacements, thickness dependence, and the effect of magnetic field and temperature on the phonon modes has not yet been studied. Such studies are significant in advancing the fundamental understanding of layered Nb_3Cl_8 and other members of the niobium halide family materials for the realization of many overarching goals in future applications.

Raman spectroscopy is used across several disciplines of science and engineering as a method of characterizing materials according to their molecular or lattice vibrations. Raman scattering results from the complex interaction between photons from an excitation source and the specific electrons and phonons in a material. Therefore a Raman spectrum is unique to each material, likening it to a 'fingerprint' of the material [9–11]. Layer-dependent Raman studies on mechanically exfoliated layered materials are useful for finding contrasts between the crystal structure of a material's bulk and thin counterparts [12–17]. Vibrational symmetries can be studied through polarization-dependent Raman spectroscopy, providing insight into the symmetries of each Raman active phonon mode in the material. Different combinations of the polarization of the excitation laser and the scattered light can be

matched to the angle-dependent intensities of the phonon modes to determine their symmetries [18–20], which then enables one to probe for structural transitions by comparing the symmetries of the phonon modes before and after the transition. The manipulation of conditions such as temperature and external magnetic field is also a reliable method of further classifying features in a characteristic Raman spectrum and determining their origins. For example, in magnetic 2D materials such as CrI_3, $FePS_3$, $GdTe_3$, and $BiSe_2/Te_3$, both temperature dependent and magneto-Raman spectroscopy have been utilized to study the effects of temperature-dependent magnetic transitions and the possible contributions of magnons in the material's Raman signature [21–24]. Varying excitation wavelength can induce second order Raman scattering via a double resonance process where the energy of the incident light matches certain electronic transitions in the material, and the momentum of the involved phonons allows quasi-horizontal electronic transitions between electronic states in different points of the Brillouin zone [25]. By exploiting resonance conditions, one can resolve Raman modes that would otherwise have intensities too low to be resolved in non-resonant conditions [26–28].

Here, we investigate the phonon dynamics of Nb_3Cl_8 in bulk and few layer flakes using Raman spectroscopy and density-functional theory (DFT) analysis to determine the material's vibrational modes, their symmetrical representation, and their atomic displacements. The manipulation of parameters such as the polarization and excitation energy of the incident beam, temperature, and external magnetic field when performing the Raman measurement provided the means to study the response of the material's phonon modes to these changes and determine the nature of the Raman active modes. We experimentally resolved 12 phonon modes, five of which are A_{1g} symmetric and seven of which are E_g symmetric. The calculated frequencies and symmetrical representations from our first principles DFT analysis agreed with our experimental observations. From the DFT results, we determined the atomic displacements of the atoms in the crystal lattice due to the Raman scattering event. Layer-dependent studies show that the Raman peak positions are mostly insensitive to changes in layer number, only slightly red shifting while peak intensity decreased and the full width at half maximum (FWHM) increased with layer thickness. Raman measurements at different excitations (473–785 nm) show the largest peak intensities when using a 473 nm excitation source, suggesting resonance between the laser's energy and the energy of an electronic transition in the material. Temperature dependent Raman measurements carried out above and below transition temperature using a 532 nm

laser did not show any changes in the symmetries of the phonon modes when compared to the high temperature phase, suggesting that the likely low-temperature phase is $R\bar{3}m$ symmetric. Magneto-Raman measurements carried out at 140 and 2 K between -2 and 2 T reveal that Raman modes are not magnetically coupled due to the absence of peak splitting, shift, or intensity loss.

2. Experimental section

2.1. Crystal growth and characterization
Single crystals of Nb_3Cl_8 were synthesized via chemical vapor transport [6] (adapted to two-zone furnace) using NH_4Cl as a transport agent. 0.1114 g Nb, 0.3639 g $NbCl_5$, and 0.0059 g NH_4Cl powders were sealed in a fused silica tube (12.75 mm OD $\times$ 10.5 mm ID) as precursors under vacuum and placed into a two-zone furnace. The furnace was ramped to 200 °C for 60 min with a dwelling time of 200 min. The precursor side and growth side were then ramped to 830 °C and 785 °C respectively for 600 min with a dwelling time of 8600 min. The precursor and growth side were then cooled to 20 °C and 350 °C respectively for 420 min and dwelled for 180 min before cooling both sides to 20 °C for 60 min. The grown Nb_3Cl_8 crystals were dark, flat, and shiny with a noticeable hexagonal shape.

Single crystal x-ray diffraction (SCXRD) measurements were carried out using a high-resolution diffractometer (Bruker D8 Discover) with Cu Kα radiation ($\lambda = 1.5418$ Å). The samples were placed on a zero-background silicon sample holder. Data were collected in the 2θ range of $10°$–$90°$ with a step size of $0.02°$ and a counting time of 10 s per step.

Magnetic susceptibility (χ) was measured using the vibrating sample magnetometer (VSM) option on a physical property measurement system (PPMS) (Quantum Design PPMS DynaCool). Samples were weighed and mounted on a non-magnetic quartz paddle sample holder using GE-7031 varnish. The same holder with only varnish was used as a blank to subtract backgrounds. Measurements were performed at temperatures ranging from 2 K to 300 K with applied magnetic fields. At each temperature, the magnetic moment was measured as a function of magnetic field by sweeping the field from -5 to 5 T, and the slope between -0.5 and 0.5 T was fitted to extract the magnetic susceptibility of the sample at the temperature.

2.2. Mechanical exfoliation of Nb_3Cl_8
Nb_3Cl_8 flakes were mechanically exfoliated from the grown bulk crystals directly onto silicon wafers with a 250 nm SiO_2 capping layer using Nitto tape (SPV-224 PVC). The flakes to be studied were then identified via optical microscopy, where color contrast and transparency were key factors in choosing the thin-layer flakes. Atomic force microscopy (AFM) was utilized to measure the thickness and identify the layer number of each flake studied during the experiment. AFM measurements taken in non-contact mode on a SmartSPM1000 scanning probe microscope. AFM measurements were taken in ambient conditions.

2.3. Raman characterization
The layer-dependent and polarized Raman experiments were performed on a confocal microscope Raman spectrometer (LabRAM HR Evolution, Horiba Scientific) using a backscattering geometry. The Raman emission was collected and dispersed by a 1800 gr mm^{-1} grating, using a 532 nm wavelength laser as the excitation source. The laser was focused on the exfoliated Nb_3Cl_8 flakes through a 100x objective (NA = 0.9, WD = 0.21 mm) with a spot size of ~ 1 μm. For the polarized Raman experiments, the polarization of the incident laser was rotated using a combination of a fixed linear polarizer (horizontally) and a rotating half-wave plate that determined the linear polarization angle, the scattered Raman signal passed through a second polarizer (analyzer) that was kept horizontal. Excitation dependent Raman spectroscopy was performed on both bulk and thin layer flakes utilizing 473 nm, 532 nm, 633 nm, and 785 nm excitation sources to probe for a resonance Raman effect in the material. These Raman measurements were performed at room temperature under ambient conditions. For the analysis of the Raman spectra, Gaussian–Lorentzian fittings were used to fit the Raman peaks and deduce the peak FWHMs, frequencies, and intensities published in this work.

Low-temperature Raman spectroscopy was performed using a backscattering geometry in a closed-cycle helium cryostat (Montana C2), and the measurements were performed in the temperature range of 7.6 K–300 K. Light from a 532 nm continuous laser (Torus 532, Laser Quantum) was focused by a 40x objective lens to a spot size of ~ 1 μm. A laser power of 1 mW was used, and the collected signal was dispersed by a spectrometer (Princeton Instruments HRS-500-MS) using a 1200 mm^{-1} groove-density grating and detected by a liquid nitrogen-cooled charge-coupled device (CCD, Princeton Instruments PyloN:400BR_eXcelon) with an integration time of 10 s. BragGrate^{TM} notch filters were used to filter out Rayleigh scattering.

Magneto-Raman measurements were carried out in a closed-cycle helium cryostat down to 2 K with split-coil conical magnet (Quantum Design Opticool) using an Andor SR-500i spectrometer and an Andor Newton DU920P BR CCD.

2.4. Calculation method
First-principles calculations were performed, utilizing the density functional theory approach as implemented in the Quantum ESPRESSO package [29]. We used norm-conserving scalar relativistic

optimized norm-conserving Vanderbilt pseudopotential [30, 31] and Perdew–Burke–Ernzerhof-type exchange-correlational functional [32], and the van der Waals correction included in the D2 formalism [33]. A primitive unit cell with two layers was fully optimized to get $a = 6.75$ Å and $c = 12.43$ Å. The convergence threshold on forces for ionic relaxation was 1×10^{-4} eV Å^{-1}. A Hubbard potential of $U = 1$ eV was used on Nb d orbitals to account for the on-site interaction [34]. Calculations were done on a $10 \times 10 \times 3$ Monkhorst-Pack k-point grid.

A density functional perturbation theory calculation was performed to calculate phonon modes. We note that electronic calculations were carried out for the interlayer antiferromagnetic stable ground state of the bulk material. However, for the Raman experiment at room temperature, the material does not have long-range magnetic order. As a result, we use nonmagnetic calculations to perform phonon calculations for the crystal system at 300 K. To test how spin polarizations would affect phonon frequencies, we performed additional calculations based on the interlayer antiferromagnetic ground states. Our calculations show that the shift of phonon energy is small ($\sim$0.2 meV on average).
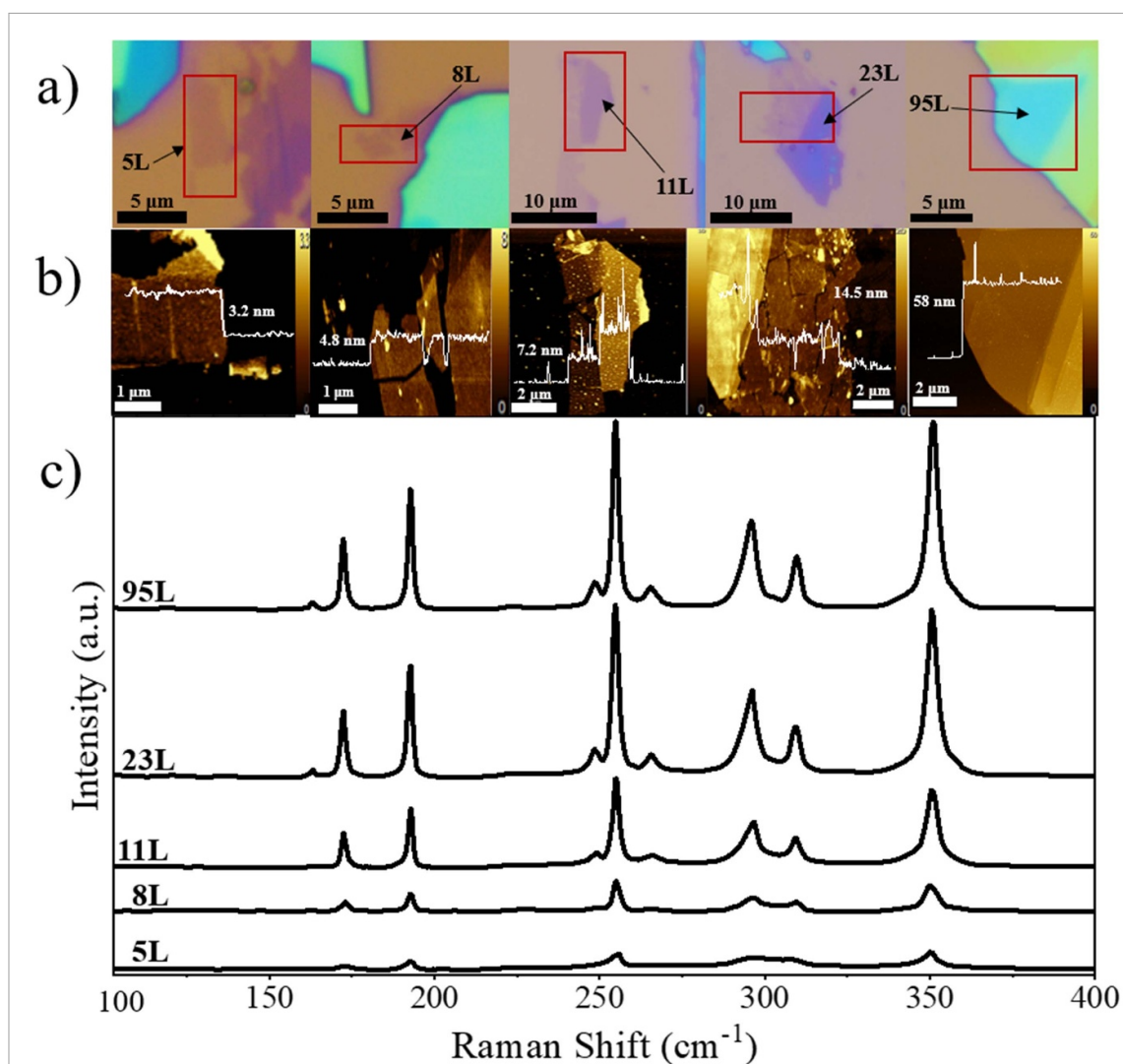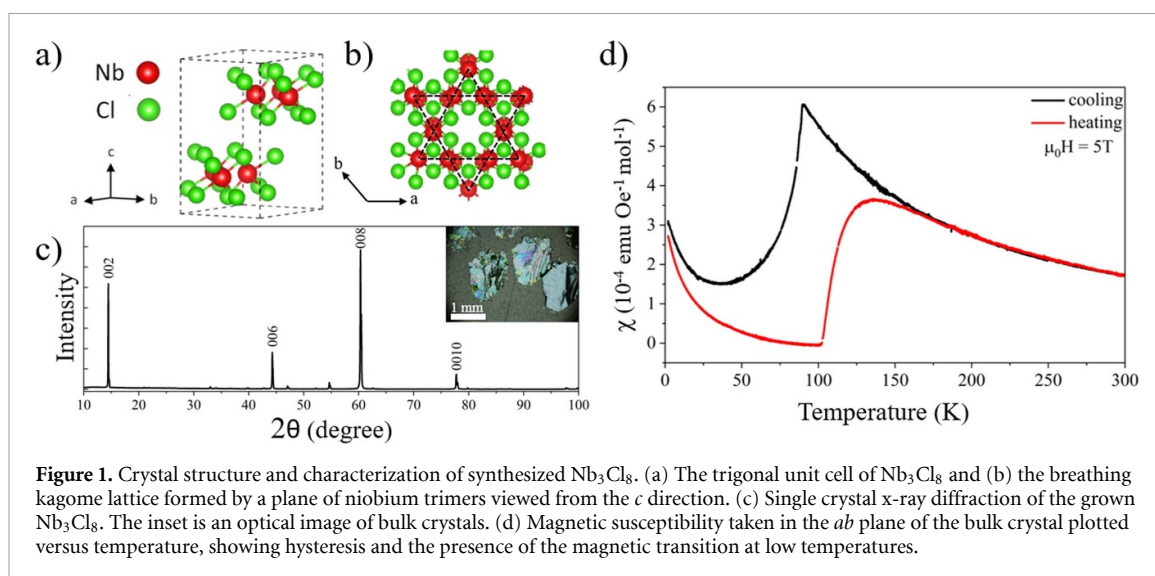
3. Results and discussion

The crystal structure of Nb_3Cl_8 as well as basic structural and magnetic characterizations of the bulk samples are summarized in figure 1. Nb_3Cl_8 crystallizes in a trigonal crystal system with space group $P\bar{3}m1$ and point group D_{3d}. Nb_3Cl_8 has been reported to have a monolayer height of 0.8 nm on SiO_2/Si, with a vertical direction (out-of-plane) lattice constant of 0.61 nm in bulk [2]. As shown in figure 1(b), the Nb_3Cl_8 crystal features a breathing kagome lattice formed by corner sharing Niobium trimers with alternating Nb–Nb distances [35, 36]. Figure 1(c) showcases the results of the SCXRD measurements taken on the bulk Nb_3Cl_8, grown using the chemical vapor transport technique described in the methods section. The sharp peaks and minimal noise indicate the good crystallinity of the sample. The periodicity of the lattice in the vertical direction is calculated to be 0.61 nm, consistent with the reported values [2]. The magnetic susceptibility of the grown crystal was then probed in a temperature cycle where the sample was first cooled down to 8 K and subsequently heated back to room temperature within a VSM. The magnetic susceptibility of the material with respect to temperature in figure 1(d) shows hysteresis between the cooling and heating transitions, with the critical cooling temperature found to be at 90 K and the critical heating temperature found to be at 103 K, both corresponding to the transition from a paramagnetic state at room temperature to a nonmagnetic singlet state [5, 6] at low temperatures. This magnetic transition has been linked to the structural phase transition
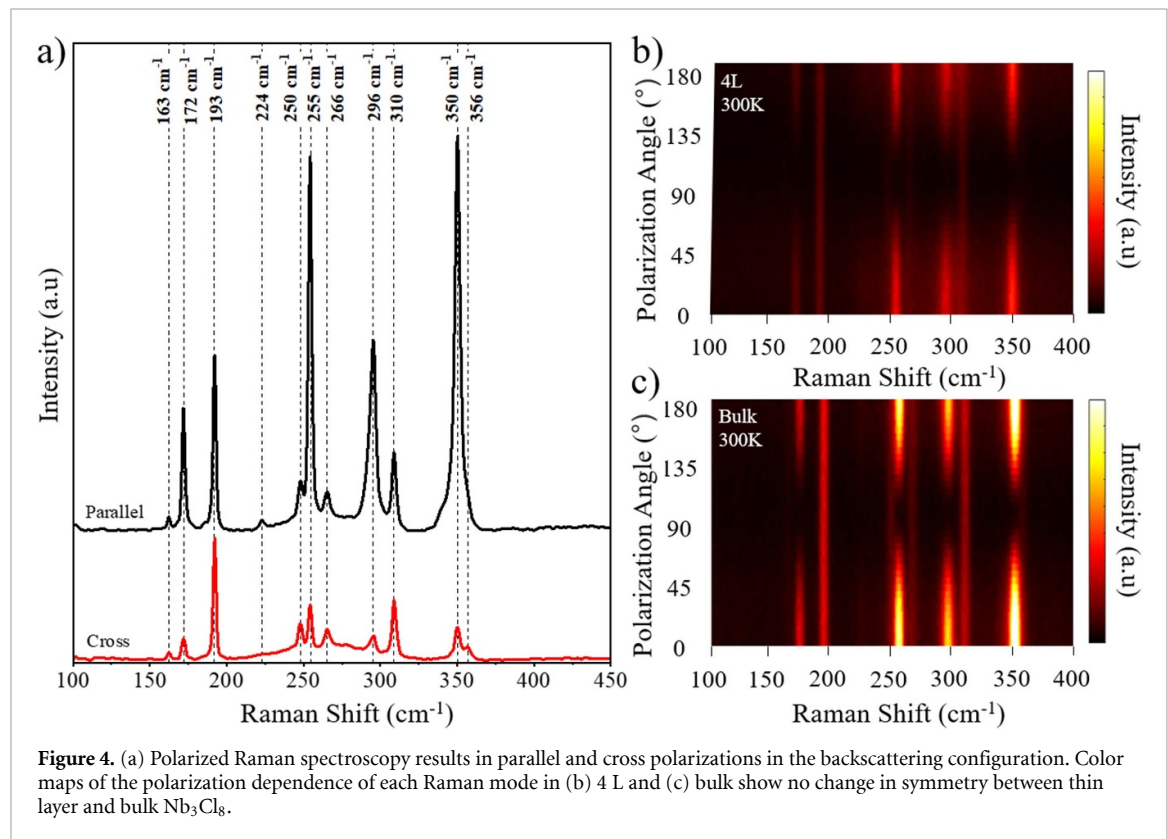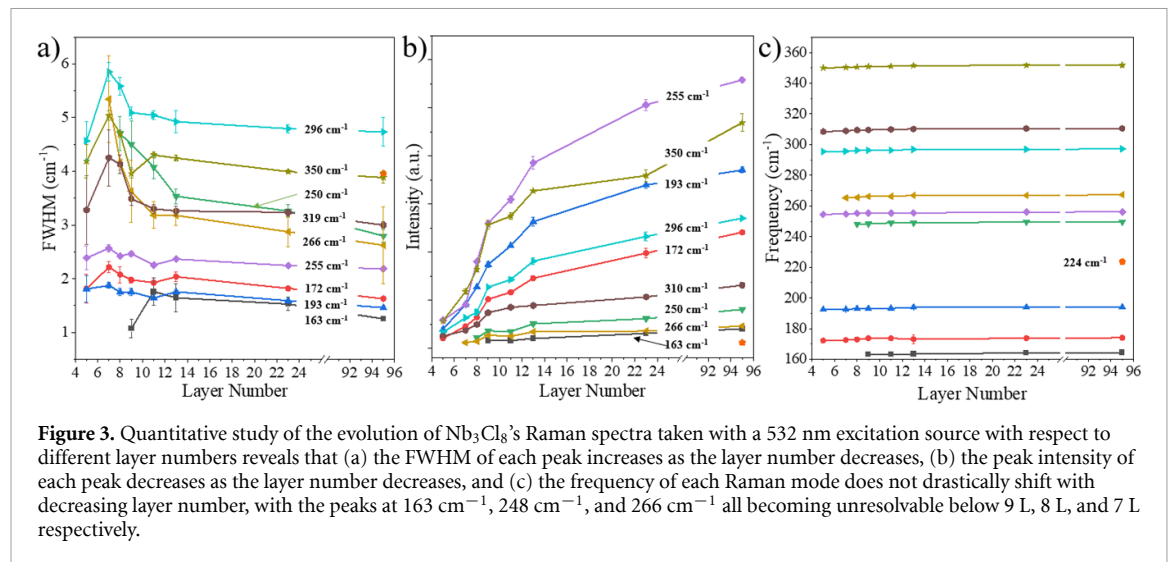
which Nb_3Cl_8 undergoes at low-temperatures in the literature, and therefore the presence of this magnetic transition in our data is the evidence that the structural transition has occurred [4–7].

3.1. Layer-dependent Raman analysis

Nb_3Cl_8 was mechanically exfoliated down to few layers using the techniques outlined in the methods section. Optical images, heights measured by AFM, and Raman spectra using a 532 nm excitation source for five different Nb_3Cl_8 flakes with various layer numbers are shown in figure 2. Figure 2(a) features the optical micrographs of flakes exfoliated onto a silicon substrate, showing that the material is a light blue color at 95 layers (95 L), dark purple at 23 L, and a light transparent purple as it is thinned down to 5 L. Using the previously cited heights, on SiO_2 and in bulk, the AFM images in figure 2(b) are used to assign layer numbers to each exfoliated flake. Changes in the Raman spectra with respect to layer number are evident in figure 2(c), where all peaks lose intensity and feature an increase in FWHM as the material is thinned down from bulk to thin layers. The Raman modes at 163 cm^{-1}, 250 cm^{-1}, and 266 cm^{-1} all become unresolvable in flakes thinner than 7 L when using a 532 nm excitation source at room temperature.

A quantitative study of Nb_3Cl_8's Raman signature at room temperature using a 532 nm excitation source and its evolution as the material is thinned down from bulk is shown in figure 3. As evident from figure 3(a), the FWHM of each peak generally increases by a minimum of about 1 cm^{-1} as the layer number decreases, with a sharp decline in 5 l due to the low intensity of each peak which is just above the noise level. Figure 3(b) exemplifies how the intensity of each Raman peak is closely related to the layer number of the flake upon which the spectrum was gathered, with the intensity decreasing as the material is thinned. Figure 3(c) reveals that none of the peaks experienced a drastic shift in wavenumber when studied from bulk to thin layers of Nb_3Cl_8, but all peaks slightly downshifted as layer number decreased (see supporting information figure S2). These redshifts can be explained by interlayer van der Waals interactions which contribute less to the phonon restoring forces as the layer number decreases, resulting in softened phonon modes [15, 37]. Figure 3(c) also shows that the peaks at 163 cm^{-1}, 250 cm^{-1}, and 266 cm^{-1} are not resolved in samples thinner than 7 L, while the peak at 224 cm^{-1} is unresolvable in thin layers. The disappearance of the peaks at 163 cm^{-1}, 224 cm^{-1}, 250 cm^{-1}, and 266 cm^{-1} as well as the decrease in intensity with layer number can be linked to the effect that an increased surface-to-volume ratio (and effectively smaller volume) will have on the cross section of evoking a Raman event. The lower probabilities to induce the Raman events will result in the

Figure 1. Crystal structure and characterization of synthesized Nb_3Cl_8. (a) The trigonal unit cell of Nb_3Cl_8 and (b) the breathing kagome lattice formed by a plane of niobium trimers viewed from the *c* direction. (c) Single crystal x-ray diffraction of the grown Nb_3Cl_8. The inset is an optical image of bulk crystals. (d) Magnetic susceptibility taken in the *ab* plane of the bulk crystal plotted versus temperature, showing hysteresis and the presence of the magnetic transition at low temperatures.

Figure 2. (a) Optical image of five different Nb_3Cl_8 flakes exfoliated onto SiO_2/Si substrates. The contrast and brightness of images were adjusted for visibility. (b) Atomic force microscopy images of the corresponding Nb_3Cl_8 flakes with inset height profiles showing the height in nanometers. (c) Raman spectra on the corresponding Nb_3Cl_8 flakes taken using a 532 nm excitation source demonstrate the evolution of the spectra as the material is thinned down from bulk to 5 L. Peak broadening, peak intensity loss, and slight peak position downshifting with decreasing layer number is observed in each peak.

Figure 3. Quantitative study of the evolution of Nb$_3$Cl$_8$'s Raman spectra taken with a 532 nm excitation source with respect to different layer numbers reveals that (a) the FWHM of each peak increases as the layer number decreases, (b) the peak intensity of each peak decreases as the layer number decreases, and (c) the frequency of each Raman mode does not drastically shift with decreasing layer number, with the peaks at 163 cm^{-1}, 248 cm^{-1}, and 266 cm^{-1} all becoming unresolvable below 9 L, 8 L, and 7 L respectively.

Figure 4. (a) Polarized Raman spectroscopy results in parallel and cross polarizations in the backscattering configuration. Color maps of the polarization dependence of each Raman mode in (b) 4 L and (c) bulk show no change in symmetry between thin layer and bulk Nb$_3$Cl$_8$.

already less intense Raman modes being drowned out by noise as the material is thinned.

3.2. Room and low-temperature polarized Raman analysis

The Raman spectra of bulk Nb$_3$Cl$_8$ measured using a 532 nm excitation source at room temperature in both parallel and cross polarizations in a backscattering configuration are shown in figure 4. As a crystal with space group $P\bar{3}m1$, Nb$_3$Cl$_8$ is expected to have 19 Raman active phonon modes [37–39]. The irreducible representations of the Raman active optical phonons in bulk Nb$_3$Cl$_8$ at the Γ point of the Brillouin zone can be expressed as $\Gamma =$ $8A_{1g} + 11E_g$. Of these 19 expected phonon modes, 11 phonon modes were experimentally resolved using a 532 nm laser (figure 4(a)) while an additional mode at 120 cm^{-1} was observed using a 473 nm laser (see figure 7), making for a total of 12 experimental phonon modes. While the results of both polarization conditions only show ten different peaks, the cross polarized configuration (red curve in figure 4(a)) showcases a shoulder peak at 356 cm^{-1} that is revealed due to the intensity loss of the 350 cm^{-1} peak, revealing the 11th phonon mode when using a 532 nm laser. Figures 4(b) and (c) provide a full Raman peak intensity map at each wavenumber as the polarization angle of the light is changed from 0°
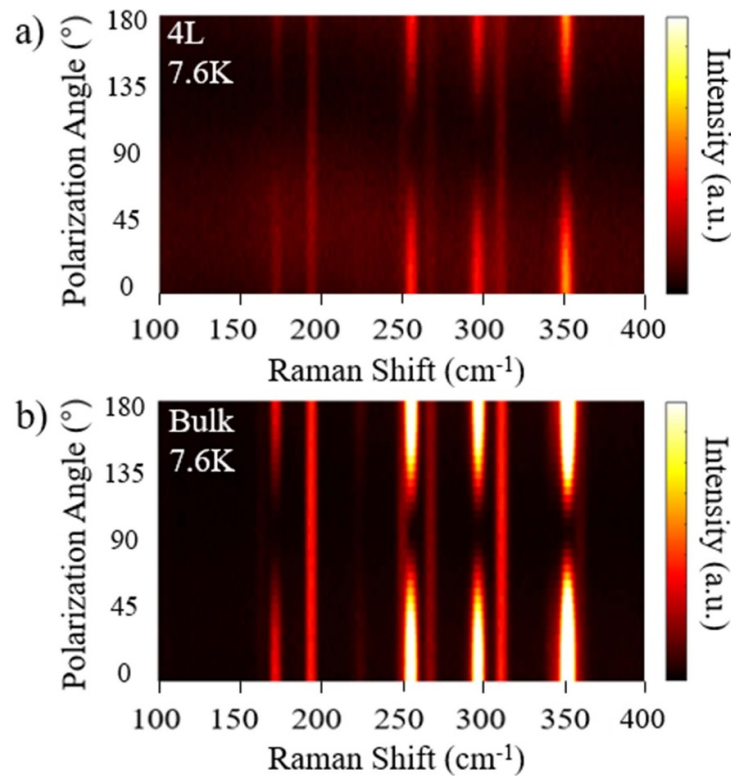
Figure 5. Low-temperature polarized Raman experiments performed on (a) 4 L and (b) bulk Nb_3Cl_8 feature no changes in the symmetries of each phonon mode in comparison to room temperature measurements.

to 180° to determine the symmetry of each phonon mode in 4 L and bulk Nb_3Cl_8, respectively. These results show no difference in the phonon symmetries between the 4 L and bulk sample, indicating a robust crystal phase regardless of layer number. As a member of the $P\bar{3}m1$ crystal space group, the Raman polarization selection rules for Nb_3Cl_8's corresponding point group, D_{3d}, were used to assign phonon peaks to their respective symmetrical representations [37–39]. The D_{3d} polarization selection rules indicate that the Raman spectra of Nb_3Cl_8 consist of A_{1g} and E_g symmetric modes. The A_{1g} modes are 'allowed' when the light reaching the Raman analyzer is linearly polarized parallel to the excitation source and 'forbidden' upon cross polarization [18, 19, 40], while the E_g modes are allowed for both configurations. Therefore, in the case where the only governing symmetries of the material's vibrational modes are A_{1g} and E_g, a comparison between the Raman spectra produced by linearly polarized and cross polarized light is sufficient to determine the symmetries of the modes present in the Raman spectra. Due to drastic changes in the relative peak intensity upon swapping polarization configurations, the peaks at 172 cm^{-1}, 224 cm^{-1}, 255 cm^{-1}, 296 cm^{-1}, and 350 cm^{-1} were determined to be representative of A_{1g} symmetrical vibrations. While the peaks at 163 cm^{-1}, 193 cm^{-1}, 250 cm^{-1}, 266 cm^{-1}, 310 cm^{-1}, and 356 cm^{-1} were found to be representative of E_g vibrations due to their

consistent intensity across all polarization configurations. These behaviors are seen in figures 4(b) and (c), most notably when tracking each peak's intensity at the 90° polarization angle, where E_g peaks have consistent intensities while A_{1g} peaks do not.

In the interest of probing the expected structural transition that Nb_3Cl_8 undergoes at temperatures lower than 90 K, polarized Raman spectroscopy above and below the transition temperature utilizing a 532 nm excitation source was performed on bulk and thin layer samples. Figure 5 details the phonon dynamics of the crystal system at low-temperatures (7.6 K) with respect to changes in polarization. In comparison to the high-temperature data from figure 4, the Raman peak intensities with respect to the polarization angles do not change in the low-temperature data, indicating that the symmetries of the phonons do not change as the crystal undergoes the structural phase transition. To interpret these results, we must revisit the controversy, mentioned earlier, that exists in the literature regarding the low-temperature phase. The structural transition was first observed in literature via diffraction data, showing that the material transitions from crystallizing at high temperature in the $P\bar{3}m1$ space group (point group D_{3d}) to crystallizing at low temperature in the predominantly $C2/m$ space group (point group C_{2h}) [4]. In this case, there is a significant change in the type of Raman active phonons expected for the

low-temperature phase (A_g and B_g) as well as the Raman tensors governing the polarization selection rules [37–39]. However, other groups have reported that the low-temperature phase corresponds to the $R\bar{3}m$ space group instead [5, 7]. Since crystals with $P\bar{3}m1$ and $R\bar{3}m$ symmetries share the same point group (D_{3d}) and hence the same Raman tensors for the A_g and E_g modes, there would be no difference in the polarization-dependence of these modes. The lack of evidence of new phonons with B_g symmetry in the 7.6 K data shown in figure 5, as well as the unchanged polarization-dependence of the Raman modes is more consistent with the low-temperature phase being $R\bar{3}m$ rather than $C2/m$.

A recent terahertz study on Nb_3Cl_8 showed that an IR-active mode at 104 cm^{-1} experiences an abrupt shift in frequency to 108 cm^{-1} as the system crossed the transition temperature of 90 K, which was claimed to be evidence of the structural phase transition from $P\bar{3}m1$ to $R\bar{3}m$ phase. We have also observed a shift in peak frequency of up to 5 cm^{-1} between 300 K and 7.6 K data for our measured peaks between 163 cm^{-1} and 350 cm^{-1} measured using a 532 nm laser (see supporting information figure S4). To investigate if the shift in frequency is abrupt as observed in [7], we present additional Raman peak position data at 140 K and 80 K for a 2 L sample (see supporting information figure S5). We note that the experiment was conducted using a different setup (Opticool) with distinct lasers and a spectrometer compared to the Raman experiment carried out at 300 K and 7.6 K (Montana C2). Nevertheless, under the same experimental conditions, we observed a maximum shift of about 1 cm^{-1} when comparing the 140 K data to the 80 K data. Although, it is not clear if a significant shift in the peak frequencies is expected between the high temperature $P\bar{3}m1$ and low temperature $R\bar{3}m$ phase for the frequency range we investigated, we cannot rule out the possibility of peak shifts in the Raman modes due to the structural phase transition. We also believe that thermal contraction of the crystal structure as the temperature decreased, has an effect on the Raman frequency shifts observed between 300 and 7.6 K.

3.3. Magneto-Raman analysis
To study the influence that an external magnetic field could have on the observed Raman modes of Nb_3Cl_8, magneto-Raman spectroscopy was carried out on a thin (2 L) Nb_3Cl_8 flake, both above (140 K) and below (2 K) the magnetic and structural phase transition temperature of 90 K. This measurement can elucidate the presence of magnon peaks, as it has been shown in literature that materials with magnetic orderings in thin layers should feature drastic peak splitting, shifting, or intensity loss [21, 22, 41, 42]. As the external magnetic field was swept between −2 T and 2 T, the intensities and frequencies of each peak were tracked. As seen in the contour plots in figure 6 and

supplementary figure S6 in the supporting information, there was no change in the intensities or frequencies of any of the Raman modes as the magnetic field strength was swept. Furthermore, no difference is seen between the high-temperature measurement in figure 6(a) and the low temperature measurement in figure 6(b), revealing that the magnetic transition also has no effect on the peak positions or general behaviors of Nb_3Cl_8's Raman modes in the presence of an external magnetic field.

3.4. Excitation-dependent Raman analysis
With absorption peaks in the visible light range, a resonant Raman effect can be expected in Nb_3Cl_8 when probed with excitation sources in the visible range. Particularly, the absorption spectrum of Nb_3Cl_8 features a broad peak between 500 nm and 400 nm [1, 2]. Considering this, an excitation-dependent Raman study in the parallel polarization configuration on the material using lasers with wavelengths in the visible range was performed in pursuit of the resonant Raman effect. The results of the excitation-dependent Raman experiment on thin layer (5 L) and bulk (60 L) Nb_3Cl_8 are presented in figures 7(a) and (b), respectively. Raman spectra were taken on the bulk and thin layer samples with four different excitation sources to probe for a resonance effect between the energies of the pumped lasers and electronic transitions within the material. In comparison to the parallel polarized spectra taken with a 532 nm source from figure 4, the 473 nm laser resolved peaks at 120 cm^{-1}, 163 cm^{-1}, 224 cm^{-1}, and 356 cm^{-1} even in thin layers. This increase in peak intensity in thin layers is evidence of the resonance effect, allowing us to resolve some of the least intense phonon modes in Nb_3Cl_8' Raman signature. Meanwhile, the Raman spectra produced by the 633 and 785 nm lasers are more difficult to resolve phonons in both bulk and thin layers. This can be due to large optical reflectance peaks Nb_3Cl_8 exhibits in the 600–800 nm range (shown in supporting information figure S3).

3.5. Density functional theory analysis
First-principles DFT calculations were utilized to compute the symmetries and frequencies of the 19 Raman active phonon modes in Nb_3Cl_8 at 300 K. Our results revealed that eight of the modes exhibit A_g symmetry while the other 11 exhibit E_g symmetry, which is in accordance with the expected number of optical phonons determined via our Raman tensor analysis. Table 1 summarizes our experimental and theoretical findings for each phonon mode, providing a comparison between the observed experimental frequencies and symmetries and those predicted via our DFT calculations. We found that the calculated values are in reasonable agreement with the experimental values from our Raman studies. The DFT analysis further allowed us to assign a vibrational symmetry of E_g to the 120 cm^{-1} mode,
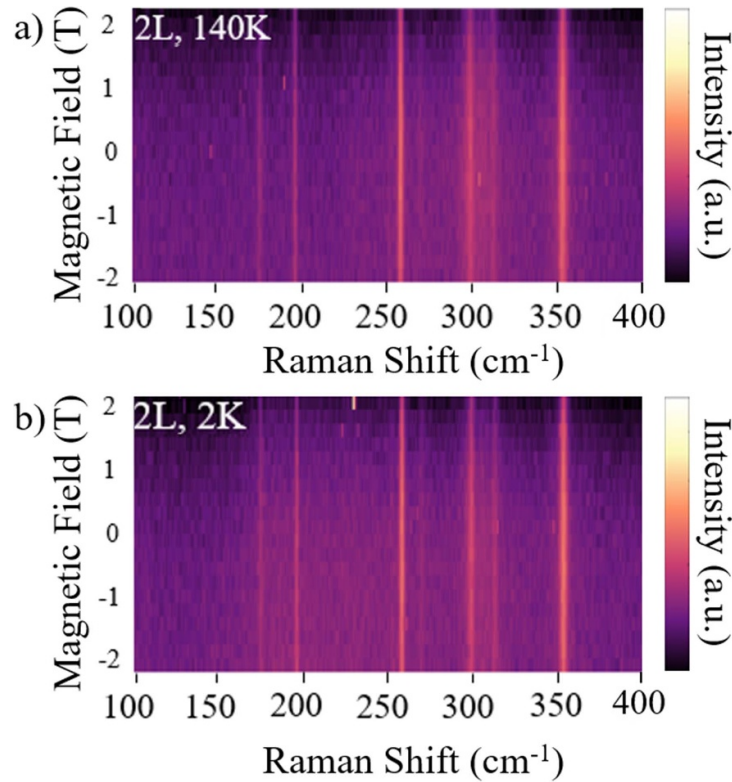
Figure 6. Magneto-Raman spectroscopy on thin layer (2 L) Nb3Cl8 shows no magnetic field influence on the Raman modes present in both the (a) high-temperature (140 K) and (b) low-temperature (2 K) measurements when the magnetic field is swept between −2 T and 2 T.
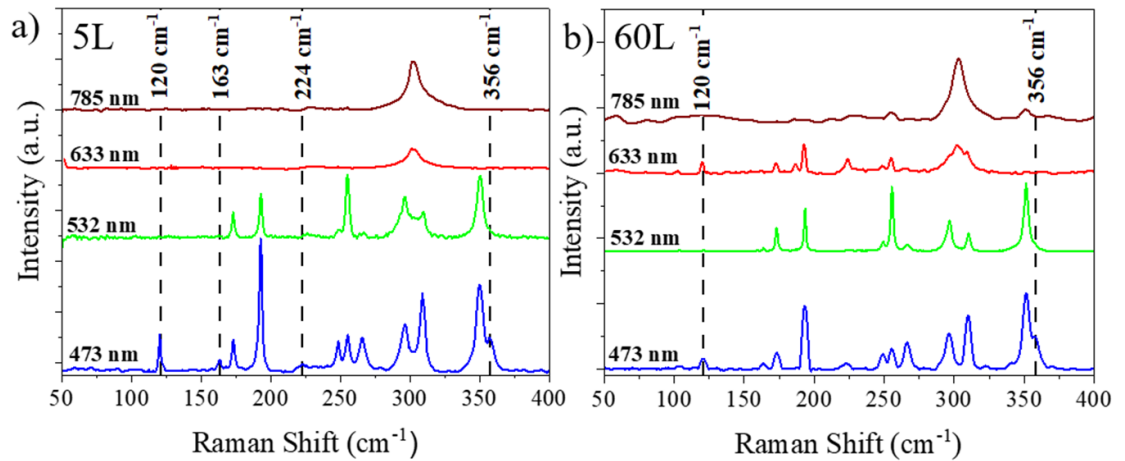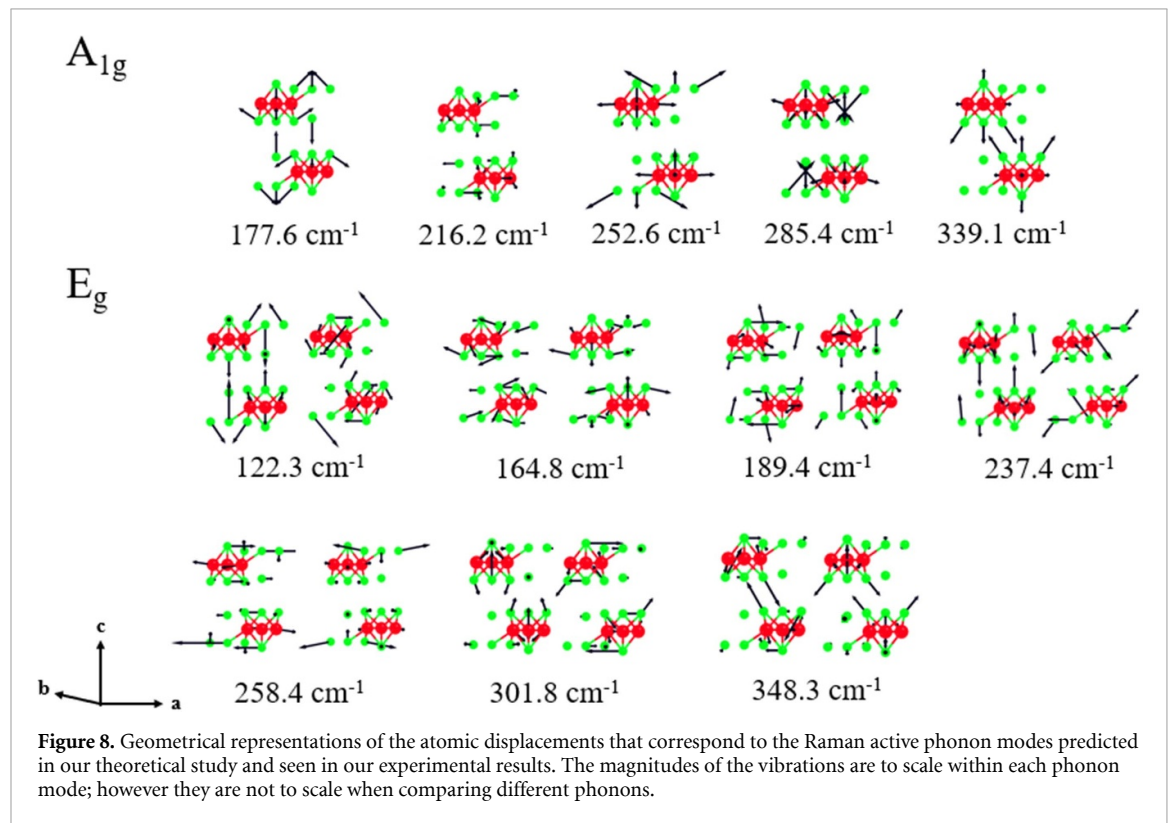

Figure 7. Excitation dependence of Nb_3Cl_8 Raman spectra utilizing 473 nm, 532 nm, 633 nm, and 785 nm excitation sources taken on a (a) thin layer and (b) bulk Nb_3Cl_8. Dashed lines indicate positions of peaks not resolved when the laser and material are not in resonance, indicating the presence of a resonance effect between the 473 nm excitation wavelength and the material.

which was only experimentally resolved under resonance conditions (see figure 7). Figure 8 provides a visualization of Nb_3Cl_8's experimentally resolved phonon modes and their corresponding atomic displacements. We modeled the atomic displacements of the 12 phonon modes and found that the seven E_g modes are vibrationally degenerate, while the other five are non-degenerate A_{1g} modes. We accentuate this distinction by showing the A_{1g} and E_g modes separately. Notably, the degeneracy is a result of

two distinct yet orthogonal vibrational modes that correspond to a single phonon. This orthogonality between the vibrations of the degenerate phonons clarifies the polarization angle-independent intensities of the E_g modes. The contrast between non-degenerate A_{1g} and degenerate E_g modes is further exemplified in our polarized Raman experiments (see figures 4 and 5), where only the degenerate E_g modes have Raman scattering intensities that are angle-independent.

Table 1. Calculated and experimental Raman active phonon modes of Nb_3Cl_8.

Calculated		Experimental	
Frequency (cm^{-1})	Irreducible representation	Frequency (cm^{-1})	Irreducible representation
27.1	E_g	—	—
48.9	A_{1g}	—	—
102.2	E_g	—	—
122.3	E_g	120.4	—
164.8	E_g	163.7	E_g
177.6	A_{1g}	173.6	A_{1g}
189.4	E_g	193.2	E_g
193.5	A_{1g}	—	—
216.2	A_{1g}	224.5	A_{1g}
216.9	E_g	—	—
237.4	E_g	250.1	E_g
252.6	A_{1g}	255.4	A_{1g}
258.4	E_g	266.3	E_g
280.5	E_g	—	—
285.4	A_{1g}	296.3	A_{1g}
301.8	E_g	310.4	E_g
339.1	A_{1g}	350.2	A_{1g}
348.3	E_g	356.8	E_g
396.1	A_{1g}	—	—

Figure 8. Geometrical representations of the atomic displacements that correspond to the Raman active phonon modes predicted in our theoretical study and seen in our experimental results. The magnitudes of the vibrations are to scale within each phonon mode; however they are not to scale when comparing different phonons.

4. Conclusion

To summarize, the effects of layer thickness, polarization, temperature, magnetic field, and excitation energy on the phonon dynamics of Nb_3Cl_8 have been investigated. Utilizing Raman spectroscopy, 12 phonon modes were resolved, of those 12, 5 were determined to be A_{1g} symmetric and seven were determined to be E_g symmetric. The frequencies, symmetrical assignments, and atomic displacements of the phonon modes calculated at room temperature via our first principles DFT analysis agreed with these experimental results. The layer-dependent studies revealed that the phonon frequencies only slightly decreased with layer number, while intensity decreased and FWHM increased more notably with layer number. Polarized Raman experiments at low-temperature show that the phonon modes do not experience any changes in symmetry when compared to those of the high-temperature phase, suggesting

that the structural phase transition is likely from high temperature $P\bar{3}m1$ phase to low-temperature $R\bar{3}m$ phase. Magneto Raman measurements show the phonon peaks did not experience any shift indicating the magnetic transition has no effect on Nb_3Cl_8's Raman modes in the presence of an external magnetic field. The Raman measurements taken at various excitation wavelengths revealed that the 473 nm excitation source exhibited the greatest resonance effect out of all the wavelengths tested. Our results provide a foundational understanding of the phonon dynamics of Nb_3Cl_8 under a variety of conditions, giving insight into the fundamental optical and vibrational properties of the crystal, as well as elucidating the effects that the low temperature structural transition has on the material's vibrational symmetries.

Data availability statement

All data that support the findings of this study are included within the article (and any supplementary files).

Acknowledgments

ORCID iDs

Dylan A Jeff ⓘ https://orcid.org/0000-0002-7761-8349
Kamal Harrison ⓘ https://orcid.org/0009-0005-5013-8547
Sabin Regmi ⓘ https://orcid.org/0000-0002-1371-3101
Zhaoyu Liu ⓘ https://orcid.org/0000-0002-9894-9622
Humberto R Gutierrez ⓘ https://orcid.org/0000-0001-8997-5274
Jihui Yang ⓘ https://orcid.org/0000-0002-5022-1771
Jiun-Haw Chu ⓘ https://orcid.org/0000-0001-6222-1210
Ting Cao ⓘ https://orcid.org/0000-0003-1300-6084
Saiful I Khondaker ⓘ https://orcid.org/0000-0003-1333-1928

References

[1] Jiang J, Liang Q, Meng R, Yang Q, Tan C, Sun X and Chen X 2017 Exploration of new ferromagnetic, semiconducting and biocompatible $Nb_3 X_8$ (X = Cl, Br or I) monolayers with considerable visible and infrared light absorption *Nanoscale* **9** 2992–3001

[2] Sun Z *et al* 2022 Observation of topological flat bands in the kagome semiconductor $Nb_3 Cl_8$ *Nano Lett.* **22** 4596–602

[3] Regmi S *et al* 2022 Spectroscopic evidence of flat bands in breathing kagome semiconductor Nb_3I_8 *Commun. Mater.* **3** 100

[4] Sheckelton J P, Plumb K W, Trump B A, Broholm C L and McQueen T M 2017 Rearrangement of van der Waals stacking and formation of a singlet state at T = 90 K in a cluster magnet *Inorg. Chem. Front.* **4** 481–90

[5] Haraguchi Y, Michioka C, Ishikawa M, Nakano Y, Yamochi H, Ueda H and Yoshimura K 2017 Magnetic–nonmagnetic phase transition with interlayer charge disproportionation of Nb_3 trimers in the cluster compound $Nb_3 Cl_8$ *Inorg. Chem.* **56** 3483–8

[6] Pasco C M, El Baggari I, Bianco E, Kourkoutis L F and McQueen T M 2019 Tunable magnetic transition to a singlet ground state in a 2D van der Waals layered trimerized kagomé magnet *ACS Nano* **13** 9457–63

[7] Kim J, Lee Y, Choi Y W, Jung T S, Son S, Kim J, Choi H J, Park J-G and Kim J H 2023 Terahertz spectroscopy and DFT analysis of phonon dynamics of the layered van der Waals semiconductor $Nb_3 X_8$ (X = Cl, I) *ACS Omega* **8** 14190–6

[8] Mortazavi B, Zhuang X and Rabczuk T 2022 A first-principles study on the physical properties of two-dimensional Nb_3Cl_8, Nb_3Br_8 and Nb_3I_8 *Appl. Phys.* A **128** 934

[9] Zhang X, Tan Q-H, Wu J-B, Shi W and Tan P-H 2016 Review on the Raman spectroscopy of different types of layered materials *Nanoscale* **8** 6435–50

[10] Liang F, Xu H, Wu X, Wang C, Luo C and Zhang J 2018 Raman spectroscopy characterization of two-dimensional materials *Chin. Phys.* B **27** 037802

[11] Cong X, Liu X-L, Lin M-L and Tan P-H 2020 Application of Raman spectroscopy to probe fundamental properties of two-dimensional materials *npj 2D Mater. Appl.* **4** 13

[12] Mañas-Valero S, García-López V, Cantarero A and Galbiati M 2016 Raman spectra of ZrS_2 and $ZrSe_2$ from bulk to atomically thin layers *Appl. Sci.* **6** 264

[13] Feng Y *et al* 2015 Raman vibrational spectra of bulk to monolayer ReS_2 with lower symmetry *Phys. Rev.* B **92** 054110

[14] Wolverson D, Crampin S, Kazemi A S, Ilie A and Bending S J 2014 Raman spectra of monolayer, few-layer, and bulk $ReSe_2$: an anisotropic layered semiconductor *ACS Nano* **8** 11154–64

[15] Li H, Zhang Q, Yap C C R, Tay B K, Edwin T H T, Olivier A and Baillargeat D 2012 From bulk to monolayer MoS_2: evolution of Raman scattering *Adv. Funct. Mater.* **22** 1385–90

[16] Jiang Y C, Gao J and Wang L 2016 Raman fingerprint for semi-metal WTe_2 evolving from bulk to monolayer *Sci. Rep.* **6** 19624

[17] Zhang X, Qiao X-F, Shi W, Wu J-B, Jiang D-S and Tan P-H 2015 Phonon and Raman scattering of two-dimensional transition metal dichalcogenides from monolayer, multilayer to bulk material *Chem. Soc. Rev.* **44** 2757–85

[18] Kim J, Lee J-U and Cheong H 2020 Polarized Raman spectroscopy for studying two-dimensional materials *J. Phys.: Condens. Matter* **32** 343001

[19] Tuschel D 2014 Practical group theory and Raman spectroscopy, Part II: application of polarization *Spectroscopy* **29** 15-22

[20] Tuschel D 2014 Practical group theory and Raman spectroscopy, part I: normal vibrational modes *Spectroscopy* **29** 14

[21] McCreary A *et al* 2020 Distinct magneto-Raman signatures of spin-flip phase transitions in CrI3 *Nat. Commun.* **11** 3879

[22] Sun Y-J, Lai J-M, Pang S-M, Liu X-L, Tan P-H and Zhang J 2022 Magneto-Raman study of magnon–phonon coupling in two-dimensional Ising antiferromagnetic FePS$_3$ *J. Phys. Chem. Lett.* **13** 1533–9

[23] Chen Y *et al* 2019 Raman spectra and dimensional effect on the charge density wave transition in GdTe$_3$ *Appl. Phys. Lett.* **115** 151905

[24] Buchenau S *et al* 2020 Temperature and magnetic field dependent Raman study of electron-phonon interactions in thin films of Bi$_2$Se$_3$ and Bi$_2$Te$_3$ nanoflakes *Phys. Rev. B* **101** 245431

[25] Berkdemir A *et al* 2013 Identification of individual and few layers of WS2 using Raman spectroscopy *Sci. Rep.* **3** 1755

[26] Fan J-H, Gao P, Zhang A-M, Zhu B-R, Zeng H-L, Cui X-D, He R and Zhang Q-M 2014 Resonance Raman scattering in bulk 2H-MX$_2$ (M = Mo, W; X = S,Se) and monolayer MoS$_2$ *J. Appl. Phys.* **115** 053527

[27] Myers Kelley A 2008 Resonance Raman and resonance hyper-Raman intensities: structure and dynamics of molecular excited states in solution *J. Phys. Chem.* A **112** 11975–91

[28] Tuschel D 2018 Exploring resonance Raman spectroscopy *Spectroscopy* **33** 12–19

[29] Giannozzi P *et al* 2009 QUANTUM ESPRESSO: a modular and open-source software project for quantum simulations of materials *J. Phys.: Condens. Matter* **21** 395502

[30] Hamann D R 2013 Optimized norm-conserving Vanderbilt pseudopotentials *Phys. Rev. B* **88** 085117

[31] Hamann D R 2017 Erratum: optimized norm-conserving Vanderbilt pseudopotentials [Phys. Rev. B 88, 085117 (2013)] *Phys. Rev. B* **95** 239906

[32] Perdew J P, Burke K and Ernzerhof M 1996 Generalized gradient approximation made simple *Phys. Rev. Lett.* **77** 3865–8

[33] Grimme S 2006 Semiempirical GGA-type density functional constructed with a long-range dispersion correction *J. Comput. Chem.* **27** 1787–99

[34] Şaşıoğlu E, Friedrich C and Blügel S 2011 Effective Coulomb interaction in transition metals from constrained random-phase approximation *Phys. Rev. B* **83** 121101

[35] Magonov S N, Zoennchen P, Rotter H, Cantow H J, Thiele G, Ren J and Whangbo M H 1993 Scanning tunneling and atomic force microscopy study of layered transition metal halides Nb$_3$X$_8$ (X = Cl, Br, I) *J. Am. Chem. Soc.* **115** 2495–503

[36] Miller G J 1995 Solid state chemistry of Nb$_3$Cl$_{18}$: Nb$_3$TeCl$_7$, mixed crystal formation, and intercalation *J. Alloys Compd.* **217** 5–12

[37] Aroyo M I, Perez-Mato J M, Orobengoa D, Tasci E, de la Flor G and Kirov A 2011 Crystallography online: Bilbao crystallographic server *Bulg. Chem. Commun.* **43** 183–97

[38] Aroyo M I, Perez-Mato J M, Capillas C, Kroumova E, Ivantchev S, Madariaga G, Kirov A and Wondratschek H 2006 Bilbao crystallographic server: I. Databases and crystallographic computing programs *Z. Fur Krist.—Cryst. Mater.* **221** 15–27

[39] Aroyo M I, Kirov A, Capillas C, Perez-Mato J M and Wondratschek H 2006 Bilbao Crystallographic Server. II. Representations of crystallographic point groups and space groups *Acta Crystallogr.* A **62** 115–28

[40] Li X, Cooper S E, Krishnadas A, Silevitch D M, Rosenbaum T F and Feng Y 2020 Optical Raman measurements of low frequency magnons under high pressure *Rev. Sci. Instrum.* **91** 113902

[41] Rigitano D, Vaknin D, Barberis G E and Granado E 2020 Raman scattering from one and two magnons in magnetoelectric LiNiPO$_4$ *Phys. Rev. B* **101** 024417

[42] Jain A *et al* 2013 Commentary: the materials project: a materials genome approach to accelerating materials innovation *APL Mater.* **1** 011002

[43] Momma K and Izumi F 2011 *VESTA 3* for three-dimensional visualization of crystal, volumetric and morphology data *J. Appl. Crystallogr.* **44** 1272–6